He, W., Zang, H., Cai, S., Mu, Z., Liu, C., Ding, M., ... & Wang, X. (2020). Intercalation and hybrid heterostructure integration of two-dimensional atomic crystals with functional organic semiconductor molecules. Nano Research, 13, 2917-2924.

Intercalation and Hybrid Heterostructure Integration of Two-dimensional Atomic Crystals with Functional Organic Semiconductor Molecules

Wen He,[a#] Han Zang,[b,c#] Songhua Cai,[b,d,e#] Zhangyan Mu,[a] Mengning Ding,[a*] Peng Wang,[b,d,f*] Xinrang Wang[b,c*]

[a] Key Laboratory of Mesoscopic Chemistry, School of Chemistry and Chemical Engineering, Nanjing University, Nanjing, Jiangsu, 210093, China.

[b] National Laboratory of Solid State Microstructures, Nanjing University, Nanjing, Jiangsu, 210093, China.

[c] School of Electronic Science and Engineering and Collaborative Innovation Center of Advanced Microstructures, Nanjing University, Nanjing, Jiangsu, 210093, China.

[d] School of Engineering and Applied Sciences and Collaborative Innovation Center of Advanced Microstructures, Nanjing University, Nanjing, Jiangsu, 210093, China.

[e] Department of Applied Physics, The Hong Kong Polytechnic University, Hung Hom, 999077 Kowloon, Hong Kong

[f] Research Center for Environmental Nanotechnology (ReCENT), Nanjing University, Nanjing, Jiangsu, 210023, China.

[#]These authors contributed equally to this work.

[*]Address correspondence to: mding@nju.edu.cn (Prof. M. Ding), wangpeng@nju.edu.cn (Prof. P. Wang), xrwang@nju.edu.cn (Prof. X. Wang).

ABSTRACT: Van der Waals (vdW) integration affords semiconductor heterostructures without constrains of lattice matching and leads to promising functional devices by design. A particularly interesting approach is the electrochemical intercalation of two-dimensional (2D) atomic crystal and formation of superlattices, which can provide scalable production of artificial vdW heterostructures. However, this approach has been limited to the use of organic cations with non-functional aliphatic chains, therefore failed to take the advantage of the vast potentials in molecular functionalities (electronic, photonic, magnetic, *etc.*). Here we report the integration of 2D crystal (MoS_2, WS_2, HOPG, WSe_2 as model systems) with electrochemically inert organic molecules that possess semiconducting characteristics (perylene-3,4,9,10-tetracarboxylic dianhydride (PTCDA), pentacene and fullerene), through on-chip electrochemical intercalation. Additional long-range spatial feature of intercalation has been achieved, which allowed facile assembly of a vertical MoS_2-PTCDA-Si junction. The intercalated heterostructure shows significant modulation of the lateral transport, and leads to a molecular tunneling characteristic at the vertical direction. The general intercalation of charge neutral and functional molecules defines a versatile platform of inorganic/organic hybrid vdW heterostructures with significantly extended molecular functional building blocks, holding great promise in future design of nano/quantum devices.

Keywords: *Transition metal dichalcogenide, Electrochemical intercalation, PTCDA, Organic semiconductor, Inorganic/organic heterostructure*

TOC

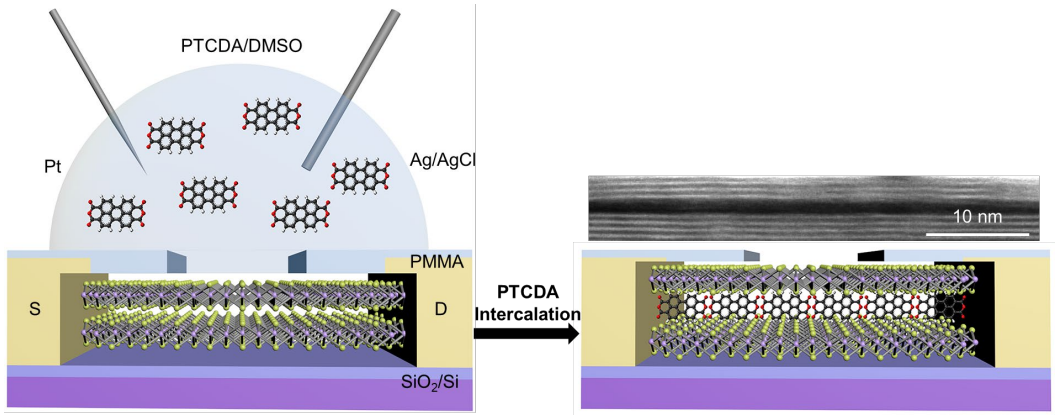

Recent advances in two-dimensional layered materials (2DLMs) have led to a set of promising applications in nano/quantum-electronics, photonics and sensors.[1-5] One distinct advantage is that they can be stacked with other dissimilar building blocks to form a large variety of van der Waals (vdW)-integrated heterostructures, creating interesting properties and functions by design.[6-8] To fully fulfill the potential of vdW-integrated systems based on 2D atomic crystals, it is critical to either achieve better control over single motif or interfacial engineering in the heterostructure,[8-19] or more effectively, to introduce new class of accessible building blocks for vdW integration. To this end, electrochemical intercalation of 2DLMs, which often results in a molecular superlattice structure with alternating monolayers of 2DLMs and intercalated ions, has become one of the most attractive integration approaches. Ion intercalation usually brings about phase transformations and slightly enlarges the layer distance,[9] with consequent increasement in electrical and electrocatalytic properties.[20, 21] More recently, molecular surfactant ions have been shown to enlarge the layer distance to a larger extent,[22-24] and further leads to the formation of

organic/2DLMs superlattice with promising properties. Successful examples include non-functional surfactant molecules and polymers such as hexylammonium chloride and CTAB.[22-25]

In a typical hybrid heterostructure or superlattice, the functionalities of organic molecules and their possible advantages to the final assemblies are yet to be explored. These potential functionalities include electronic or photonic properties from well-defined HOMO/LUMO structure in semiconductor molecules, magnetic properties from electron spins in radicals or coordination compounds, and non-linear characteristics from asymmetric compounds, *etc.* Integration of these functionalities and 2DLMs at molecular level, that is, to achieve the 2D atomic crystal/functional molecular monolayer heterostructure/superlattice, is therefore of fundamental and practical significance.

Here we demonstrate the 2D atomic crystal/functional organic molecule heterostructure achieved by electrochemical intercalation of 2DLM with organic semiconductor molecules that possess intrinsic electronic/photonic characteristics. Typical vdW TMD crystals with excellent performance of charge transport (MoS_2, WS_2, HOPG, WSe_2)[1, 26] and widely employed organic semiconductors that owns excellent optical properties (perylene-3,4,9,10-tetracarboxylic dianhydride (PTCDA), pentacene and fullerene),[27] were selected as proof-of-concept building blocks in this study. The alternating layers of MoS_2 and PTCDA were confirmed by cross-sectional scanning transmission electron microscopy (STEM) high angle annular dark field (HAADF) imaging, with layer-by-layer electron energy loss spectroscopy (EELS) evidence of strong interfacial electronic coupling. The heterostructure exhibits a heavily doped metalloid behavior, which is in distinct contrast to inorganic or surfactant ion intercalation,[9, 22, 23] and leads to a significantly improved TMD-metal contact. The PTCDA intercalation also demonstrate a long-range pathway, offering extra advantage for remote modification of comprehensive

heterostructure configuration, such as selective modulation of covered layer in vertical junctions, or the construction of single molecule vertical transistors sandwiched by 2DLM contact. The general principle of functional and charge neutral molecular intercalation could be extended to numerous vdW integrated heterostructures, with abundant choice of 2DLMs and organic molecules with specific functionalities.

RESULTS AND DISCUSSION

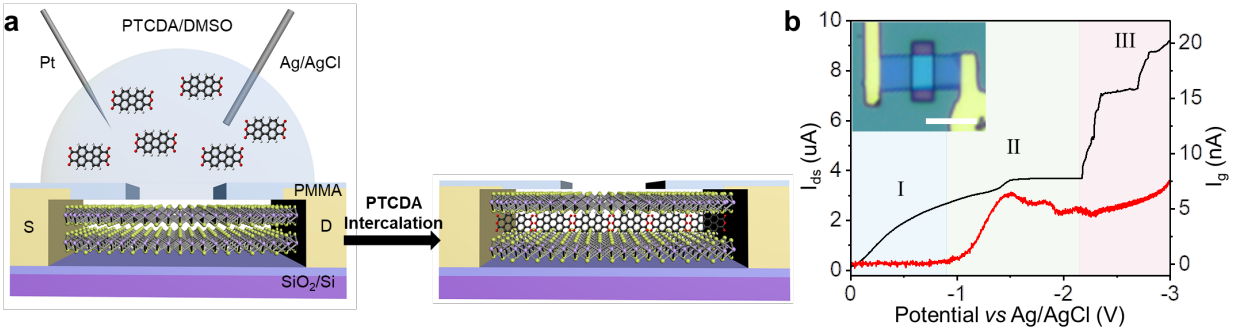

Figure 1. On-chip electrochemical intercalation. (a) Schematic illustration of the on-chip electrochemical intercalation platform. (b) The on-chip *in situ* monitoring of the electrochemical intercalation of PTCDA, with electrochemical (red) and concurrent electrical transport (black) measurements. Inset depicts the optical microscopic image of the device, scale bar is 5 um.

For intercalation, selected area of MoS_2 channel was exposed to electrolyte as working electrode of an on-chip microchemical cell, as illustrated in Figure 1a. More details of the device fabrication, on-chip electrochemical and ETS measurements can be found in the Methods and Supplemenatry Fig. S1. It is worth noticing that electrolyte is generally a necessary component in a typical electrochemical reaction (including intercalation). In our system, SDS can be used the electrolyte. However, as shown in Supplementary Fig. S2, the on-chip electrochemical

intercalations occur regardless of the presence of electrolyte. To simplify our methodology, electrolytes were therefore not employed in all subsequent electrochemical reactions in this study.

With recently developed Electrical Transport Spectroscopy (ETS),[28-30] the intercalation process can be continuously monitored *via* both electrochemical (gating) and channel conductance current, allowing for precise control in this system. Results in Figure 1b represent the typical electrochemical intercalation current (red curves) and concurrent channel conductance (ETS) result (black curve) of a few-layer MoS_2 device during PTCDA intercalation. The obvious gate (Faradaic) current after the onset potential at ~-0.9 V (*vs* Ag/AgCl), indicates the general electrochemical reduction of the system. The conductance of MoS_2 also show a step-wise increase (Figure 1b black curve) when the electrochemical potential of MoS_2 was continuously swept from 0 to -3 V (*vs* Ag/AgCl), indicating a successful intercalation of PTCDA molecules. The ETS profiles during PTCDA intercalation consist of three distinct stages: Stage Ⅰ at relatively lower potentials with graduate and slow increase of conducting current until a steady state (blue area in Figure 1b), which can be attributed to the ionic-gating effect of the semiconducting MoS_2 channel *via* electrochemical double-layer (the MoS_2 device shows a typical *n*-type semiconductor characteristic with an on/off ration of 10^6);[31] Stage Ⅱ where an obvious electrochemical (gate) current starts to emerge (green area in Figure 1b), indicating the onset of an electrochemical transition; and Stage Ⅲ with an abrupt and stepwise increase of the conductance after the onset potential of ~-2.1 V *vs* Ag/AgCl (pink area in Figure 1b). The abrupt increase of the I_{ds} in stage Ⅲ reveals the significant conductance modulation of MoS_2 due to the molecular intercalation (PTCDA) into van der Waals gaps of the MoS_2 nanosheet. More interestingly, the stepwise characteristic observed in the lateral channel conductance indicates a quantized feature of the MoS_2 intercalation: during electrochemical intercalation process, the

entering of PTCDA molecules and consequently induced phase transition of MoS_2 (from 2H-phase to metallic 1T-phase) are likely to follow a layer-by-layer process,[9] with a fine distinction in the driving force (electrochemical potential), due to the slight energy difference between different layers. The working principle of this approach (2DLMs intercalation with charge neutral functional molecules) opens vast opportunities in the functional inorganic/organic vdW heterostructures, with potentially tunable electronic, photonic, or magnetic properties from various molecular functionalities.

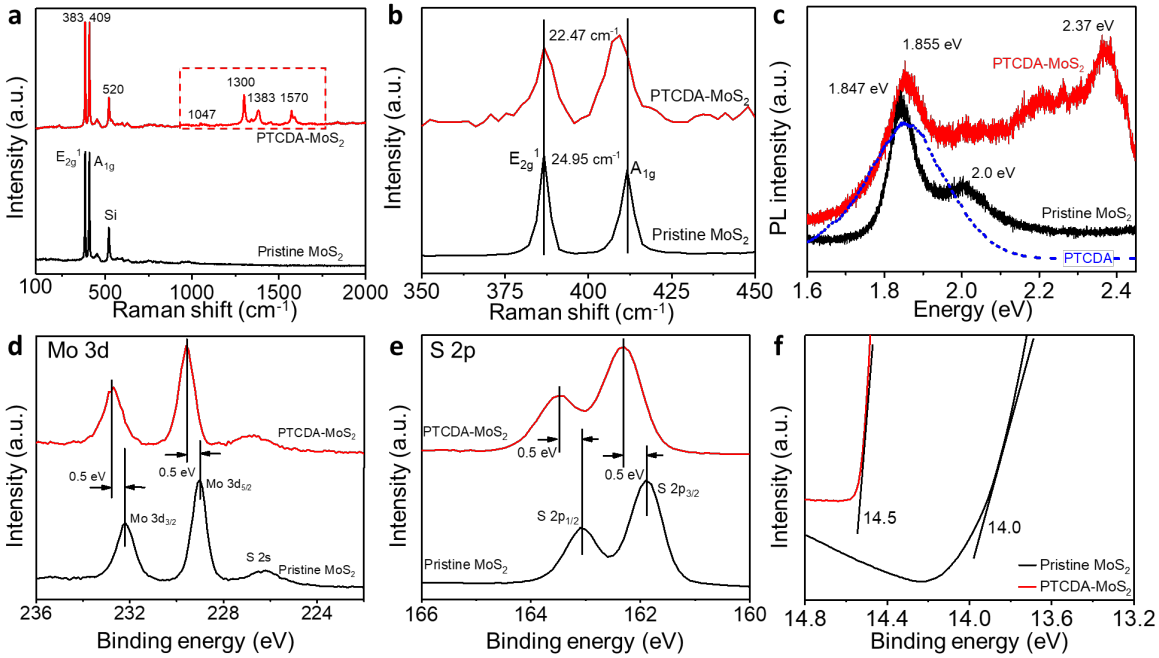

Figure 2. Evolution of spectroscopic characteristics of MoS_2 upon PTCDA intercalation. (a) Raman spectra of MoS_2 before (black) and after (red) electrochemical intercalation of PTCDA. (b) Raman spectra of the E_{2g} and A_{1g} peaks of MoS_2 before (black) and after (red) intercalation. (c) Photoluminescence (PL) spectra of pristine MoS_2 (black) and PTCDA-intercalated MoS_2 (red), and freely suspended PTCDA molecules (blue dashed line) respectively. (d, e) X-ray photoelectron spectroscopy (XPS) Mo 3d (d) and S 2p (e) spectra of MoS_2 before (black) and

after (red) intercalation. (f) Ultraviolet photoelectron spectroscopy (UPS) results of the pristine MoS_2 and PTCDA-intercalated MoS_2 in secondary electron cutoff binding energy.

Spectroscopic characterizations were further applied to confirm and analyze the molecular intercalation between PTCDA and MoS_2 layers. The Raman spectrum in Figure 2a shows that the intercalated sample exhibits clear new peaks between 600-1600 cm^{-1}, in addition to those corresponding to in-plane E_{2g} and out-of-plane A_{1g} vibration of MoS_2,[32] which can be attributed to the intercalated PTCDA molecules and are consistent with the theoretical predictions.[33] Meanwhile, the E_{2g} peak of MoS_2 remained unchanged while the A_{1g} peak shifted to a lower wavenumber with obvious broadening (Figure 2b). It should be noted that although the abrupt and stepwise feature in the lateral conductance change agrees with a semiconducting 2H to metallic 1T phase transition of MoS_2 from intercalation (which is also the general case in inorganic/organic ion intercalation),[23, 25] different observations were obtained in Raman results. The typical characteristic vibration peaks corresponding to metallic MoS_2 (J1, J2, J3) were not observed, instead, the electron-phonon scattering of the A_{1g} vibration became stronger comparing to the E_{2g} vibration upon PTCDA intercalation.[34] Such inconsistence can be attributed to the low stability of stress-induced 1T-MoS_2,[12, 35] after immediate phase change during intercalation (revealed by *in situ* electrical measurements),[25] consequent phase relaxation from meta stable 1T to 2H determines the Raman characteristics. Therefore, an overall chemical doping effect of the MoS_2 was observed,[13] suggesting a distinct electronic intercalation between the MoS_2 layer and intercalated PTCDA. To further confirm the PTCDA interactions and investigate its electronic coupling with the adjacent MoS_2 layer, photoluminescence (PL) and photoelectron spectroscopy were conducted and results are shown in Figure 2c-f. The PL characteristics of MoS_2 before and after PTCDA intercalation can be found in Figure 2c. New

emissions were observed at ca. 2.37 eV, with two MoS_2-originated peaks at 1.85 and 2.0 eV. The significantly blue-shifted emissions can be attributed to the ordered molecular assembly of PTCDA between the MoS_2 lattice, and blue-shifts coincide with the typical PL characteristics from the H-aggregates of PTCDA molecules (a "side-by-side" orientation and the resulted positive inter-molecular Coulomb coupling),[36] as opposed to the J-aggregates (a "head-to-tail" orientation and negative Coulomb coupling) from typical organic crystal lattice. We further employed X-ray photoelectron spectroscopy (XPS) to probe the change in the electronic structures of MoS_2 upon PTCDA intercalation. As shown in Figure 2d and 2e, both Mo 3d and S 2p peaks shift to a higher binding energy (~0.5 eV, an opposite direction as in the case of phase transitions),[12] indicating that the Fermi level of MoS_2 moves closer to the conduction band, *i.e.*, a *n*-type doping presumably induced by the electronic interactions with intercalated PTCDA molecules. Such heavy doping potentially causes a considerable drop of Schottky barrier height between the metal and MoS_2 device,[37] and could therefore significantly reduce the contact barrier in a typical MoS_2-based device.[38] Ultraviolet photoelectron spectroscopy (UPS) was also used to investigate the influence of PTCDA on the chemical structure and energy level of MoS_2. As shown in Figure 2f, the secondary electron cutoff binding energy of the intercalated sample shows a 0.5 eV shift towards higher binding energy, confirming a reduction of the work function and the change of vacuum level,[14] as a result of the doping effect after intercalation.

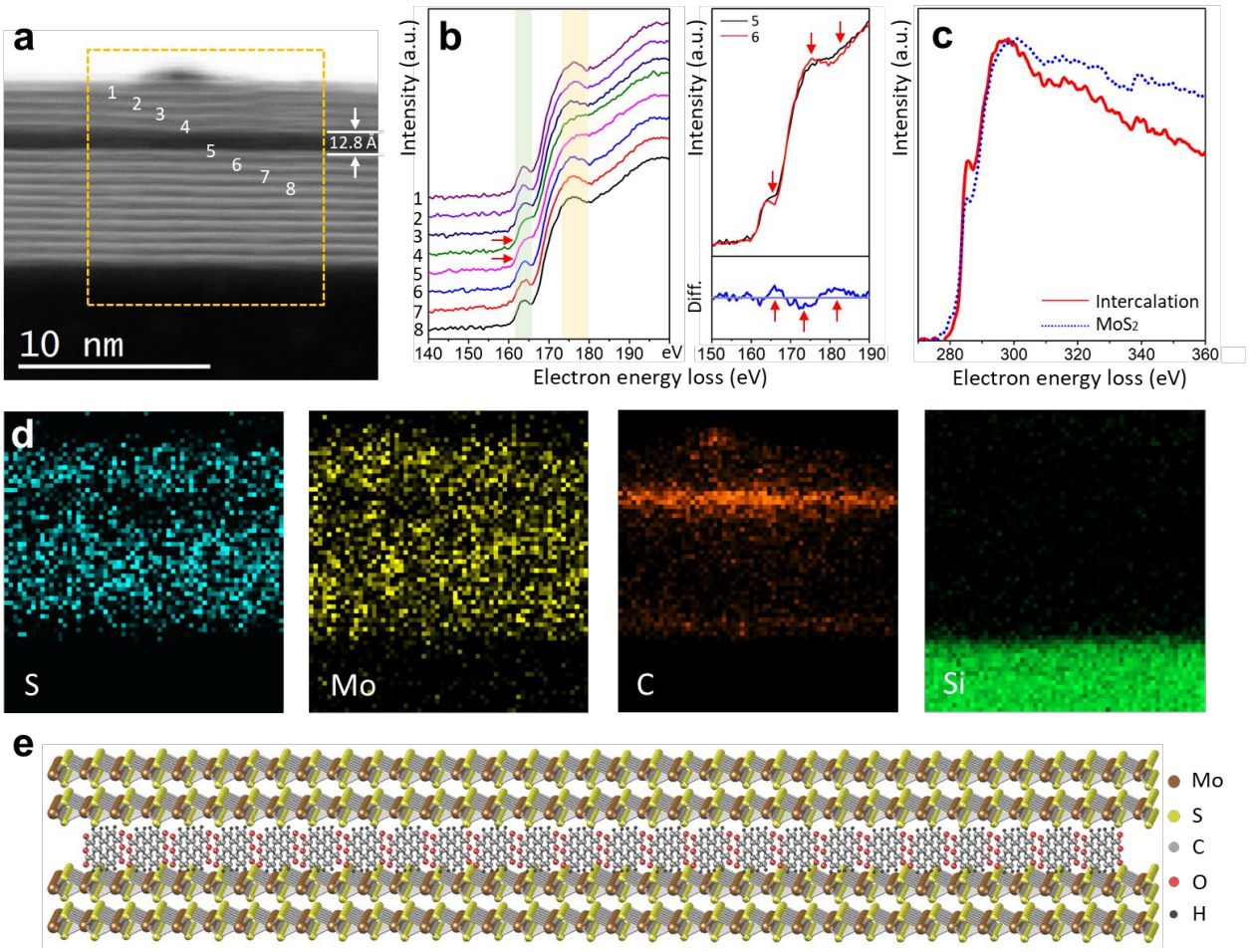

Figure 3. Structural and elemental analysis of PTCDA-MoS_2 heterostructure. (a) Cross-section STEM-HAADF image of a MoS_2 device after PTCDA intercalation. (b) Fine structure of sulfur's electron energy loss edge from eight MoS_2 layers marked in (a), the two peaks of S $L_{2,3}$ edge at 165 eV and 175 eV disappears in the 4th and 5th spectra. Right part shows the difference between the 5th and 6th spectra (indicated by two red arrows) with an offset in the range from 164 eV to 187 eV in Diff spectrum. (c) Carbon's electron energy loss edge obtained from the regions with intercalated organic molecules (red) and other regions of MoS_2 with amorphous carbon contaminated (blue). *a.u.*, arbitrary units. (d) Corresponding STEM-EELS elemental mapping (S, Mo, C, Si and O elements). (e) Schematic of PTCDA intercalation.

Detailed microstructural analysis of the vdW integration of MoS_2 and PTCDA were further carried out on a cross-section sample using high spatial resolution STEM in combination with high energy resolution EELS. The cross-sectional sample was prepared by focused ion beam (FIB). Details of the sample preparation and microscope settings can be found in Methods. Utilizing an aberration corrected electron probe, STEM-HAADF image is able to reveal real-space structure of the superlattice with atomic resolution.[19, 39] Figure 3a depicts a typical STEM-HAADF image of a cross-sectional sample of PTCDA-intercalated MoS_2 on Si substrate. As the HAADF signal is monotonically proportional to the atomic number (Z), the contrast of the PTCDA layer was darker than that of MoS_2 due to the higher atomic number of Mo and S, suggesting the PTCDA intercalation between the MoS_2 layers. A tremendous lattice expansion was observed between MoS_2 5^{th} and 6^{th} layer, clearly indicating the intercalation position and extent. The layer distance increased from 6.4 Å to 12.8 Å, corresponding to one layer of standing PTCDA molecules (landscape), as illustrated in Figure 3e. In addition, MoS_2 samples with different levels of PTCDA intercalation can be observed with larger electrochemical potentials or longer reaction time. Fig. S3 and Fig. S4a demonstrate a variety of PTCDA intercalated MoS_2 with interlayer distances of 19.0 Å, 23.9 Å, 29.8 Å, 36.2 Å, 42.5 Å. These lattice expansions demonstrate a step increment of about 6 Å, which is consistent with the landscape height of the PTCDA molecule.[36]

Furthermore, high energy resolution EELS was conducted to acquire elemental and chemical state information. STEM-EELS elemental mapping (Figure 3d) shows spatial distribution of S (blue), Mo (yellow), C (green) and Si (green) elements across the heterostructure sample. A strong carbon signal in C K-edge mapping confirmed the accumulation of organic substance at the intercalation position in Figure 3a. In addition, the elemental distribution of sulfur,

molybdenum, silicon and oxygen also consisted with the MoS_2 structure. To further probe the electronic modulation of the MoS_2 layers. ELNEs of the S $L_{2,3}$-edge and C *K*-edge (corresponding to MoS_2 and PTCDA, respectively) at the intercalation region was performed to reveal the layer-by-layer valance change of the two elements. The spectra of the S $L_{2,3}$-edge acquired from a series of positions across the intercalation layer (layers 1-8 in Fig. 3a) are shown in Fig. 3b. The ELNES of the S $L_{2,3}$-edge shows a noticeable change at two MoS_2 layers adjacent to the intercalated PTCDA. The disappearance of characteristic peak of S $L_{2,3}$ edge both at 165 eV and 175 eV indicates a chemical state change in MoS_2,[40, 41] presumably induced by PTCDA intercalation and consequent electron transfer from PTCDA to the MoS_2 layer. The ELNES of the C *K*-edge acquired at PTCDA layer in Fig. 3c shows a major peak shift from 301 eV (with amorphous carbon contaminations from other positions) to 297 eV, which is characteristic to the partial electron depletion of carbon in the PTCDA molecule (due to the existence of C=O bond)[42, 43] and further confirms the PTCDA intercalation. Together these results verify the uniform intercalation of PTCDA, the intact structure of MoS_2 layers in the heterostructure, and more importantly, a strong electronic coupling between PTCDA and adjacent MoS_2 layers that leads to partial charge transfer at the interface. With more reaction time, the PTCDA intercalation proceeds to a larger extent (a uniform thickness increasement of 19.0 Å, corresponding to 2 molecular layers, see Supplementary Fig. S4), indicating the possible control of molecular layers in this vdW integration scheme.

Results from both *in situ* electrical measurements and the chemical states of each layer in the resulting heterostructure can help deduct the details of the intercalation process. Due to the specificity of the electrochemically inert and charge neutral PTCDA molecules, the electrochemical intercalation should follow similar reaction path as typical cation intercalations

(Li^+ or cetyltrimethylammonium) of 2DLMs, but with slight difference regarding charge balance for neutral molecules. The intercalation occurs at a cathodic potential, where the layers of MoS_2 can be negatively charged and opens a gap by the repulsive force (it is interesting that anodic intercalation has not been observed in our studies, nor has any example been reported in literature). PTCDA molecules can then enter the layers of MoS_2 acting as a charge buffer to partially stabilize the negatively charged MoS_2 layers (as a result, PTCDA is partially reduced, as also indicated by UV-vis spectroscopy, see supplementary Fig. S5), and therefore lead to intercalation and consequent strong electronic interactions between intercalated PTCDA molecules and adjacent MoS_2 layers (indicated by fine structure EELS, Figure 3b). To further verify the proposed mechanism, control experiment was carried out with MoS_2 device in pure organic solvent (*i.e.*, DMSO). As shown in Supplementary Fig. S6, the on-chip CV indicates similar intercalation process with sole solvent molecules, and the intercalated MoS_2 device exhibit a weak *n*-type doping. It should be noted that for well-established cationic intercalations of 2DLMs, generally accepted mechanism involves the negative charging of 2D layers and consequent cation entrance *via* Coulomb forces.[20, 22, 23]

In order to further probe the intercalation mechanism, and to test the generality of this methodology for the construction of artificial heterostructure/superlattice, we have further screened WS_2, HOPG, WSe_2 as 2DLMs for the intercalation of pentacene and C_{60} as organic semiconductor molecules, results were summarized in Supplementary Fig. S7 to S9. MoS_2 and WS_2 are *n*-type semiconductors, WSe_2 is *p*-type semiconductor, and HOPG presents the bipolar characteristics. In all electro-intercalation systems, the on-chip electro-intercalations resulted in a general *n*-doping, which further confirmed the doping effect of cathodic process regardless of the 2DLMs and organic molecules. The doping level of these systems appear differently, indicating

distinct effectiveness of the electro-intercalation with specific combination of 2DLMs and organic molecules. Based on the previously deduced mechanism (cathodic gap opening of 2DLMs with following entrance of molecules), the corresponding electrochemical features during intercalation process should be independent of the organic molecules but closely related to the type of 2DLMs. Indeed, for the same molecule with different 2DLMs, distinct electrochemical characteristics were observed, further confirming that the intercalation process is not through a pre-electrochemical reduction of organic molecules. In addition, reduction peaks for the same 2DLMs demonstrated some resemblance for different molecules, but not with exact same feature (Fig. S7 and S8). This result indicates that even though the functional organic molecule is not reduced before intercalation, it still participates in the gap opening stage, presumably with solvent molecules.

Overall, our results suggest that the electrostatic attractions might not necessarily be the only driving force for the molecular intercalation. When the electrochemical potentials are negative enough to overcome the vdW force barrier and open the interlamellar gap of 2DLMs, neutral organic molecules (presumably with electron acceptor characteristics) are capable of entering the charged vdW gap and form a relatively more stable heterostructure. This working principle holds great promise for the potential development of hybrid functional heterostructures, utilizing a variety range of neutral organic molecules with intrinsic electronic, photonic, or magnetic functionalities.

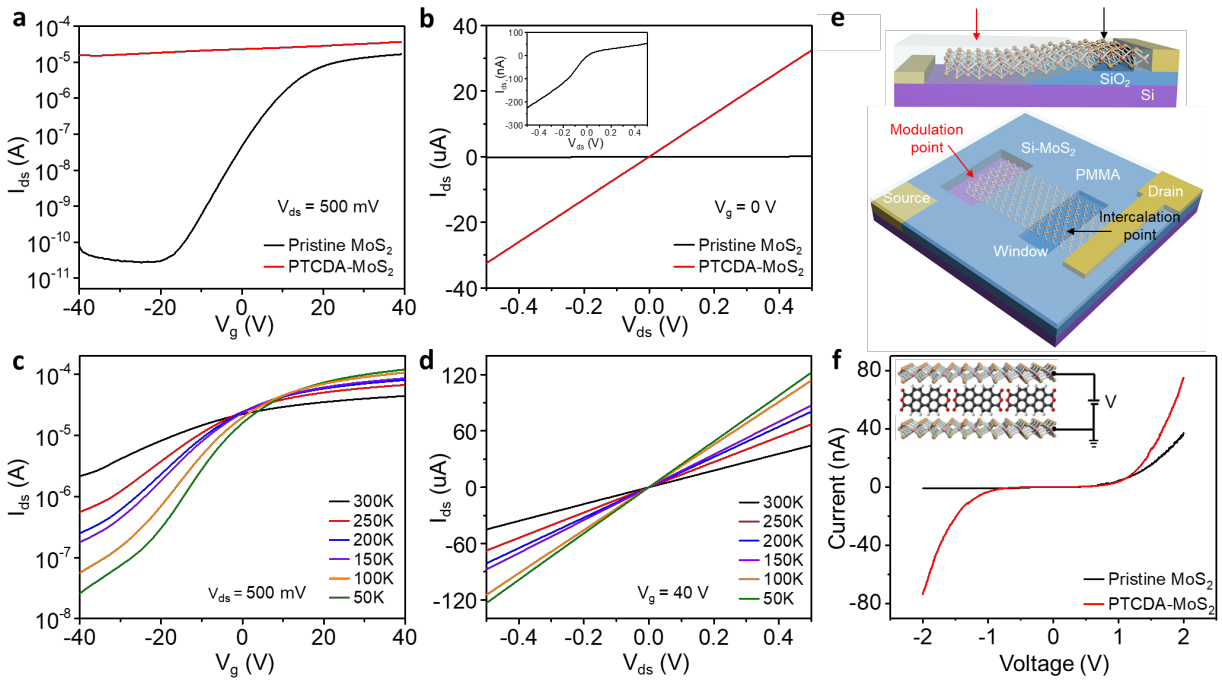

Figure 4. Evolution of lateral electrical properties from MoS_2 to PTCDA-MoS_2 and vdW integration of vertical junctions *via* on-chip long-range electrochemical intercalation. (a, b) Transfer and output characteristic curves of a typical MoS_2 field-effect-transistor (FET) device before (black) and after intercalation (red). (c, d) Transfer and output characteristic curves of the MoS_2 FET device after PTCDA intercalation at the temperature range of 50K-300K. (e) Schematic illustration of the construction of Si-MoS_2-PTCDA-MoS_2-Au vertical junction, with an electrochemical intercalation window in a distant location from the resulting active junction. (f) Electrical properties of a Si-MoS_2-PTCDA-MoS_2-Au vertical junction before (black) and after (red) PTCDA intercalation, showing the evolution from a typical *p-n* junction to a vertical molecular tunneling characteristic, inset depicts the side view of the final vertical molecular junction.

The modulation of 2D atomic crystals within a vdW-integrated system is one major motivation for the development of functional approaches such as electrochemical intercalation.

To this end, the evolution of electrical properties from MoS_2 to PTCDA-intercalated heterostructure have been systematically investigated. The as-fabricated MoS_2 field effect transistors (FETs) using Ti/Au as contact electrodes were firstly measured in vacuum. Figure 4 demonstrates the transfer and output characteristic curves of a typical MoS_2 FET device (back gate, 275 nm SiO_2) before and after PTCDA electrochemical intercalation. The transfer curve of pristine MoS_2 in Figure 4a shows a typical *n*-type semiconductor with on/off ratio up to 10^6. Similar with the common problems of pristine MoS_2-based device with metal contacts, an obvious contact barrier was observed, resulting in a non-linear I-V curves (Figure 4b). As confirmed by our spectroscopic characterizations, the PTCDA intercalation induces a heavy doping effect as a result of the strong electronic coupling (charge transfer) between PTCDA molecules and adjacent MoS_2 layer. This interaction can be potentially employed as an efficient modulation approach for the *in situ* degenerate doping of the MoS_2 and/or the elimination of the contact resistance in a typical MoS_2-based device. Indeed, after the on-chip intercalation, the transfer curves (Figure 4a red line) of a MoS_2 device can be altered to a nearly gate-dependence-free behavior, and the on-current has an order of magnitude increase as to the pristine device, a typical behavior of the degenerately doped (*n*-type) semiconductor. Meanwhile, the output curve of the PTCDA intercalated MoS_2 also changed dramatically, a significantly increased output current and much linear behavior can be observed from the PTCDA intercalation (Figure 4b), indicating almost diminished metal-MoS_2 contact barrier upon PTCDA intercalation. For the current work, it is sufficient to point out that the electrochemical intercalation causes charge transfer between MoS_2 and PTCDA to make MoS_2 itself reaching a degenerate *n*-type doping.

For general intercalation of different 2DLMs with different organic molecules, while all intercalated systems demonstrate a *n*-doping effect to the 2DLMs, it is interesting that some lead

to a strong degenerate doping and some just result in a mild *n*-doping (see Supplementary Fig. S7 and S8). We further noticed a close correlation between the second electrochemical reduction stage and the final doping level of 2DLMs. For all the relatively strong doping (MoS_2-PTCDA, MoS_2-Pentacene, MoS_2-C_{60}, WS_2-PTCDA, HOPG-PTCDA, HOPG-C_{60}) systems, a clear second stage of electrochemical reduction currents can be observed (see Supplementary Fig. S7). Similar behavior was also observed for *p*-type WSe_2 (Fig. S9). After the first electrochemical reduction stage where the interlamellar gap of 2DLMs is opened, the neutral molecules are intercalated to a greater extent during the second electrochemical stage, and as a result the electrical performance is strongly doped. We further noticed a *p*-doping behavior for C_{60} doped WSe_2 (Fig. S9) and SDS doped MoS_2 (Fig. S10). This observation indicates a potentially extended scope of tunability for heterostructures constructions, which requires further mechanistic investigation. Based on the similar principle, intercalation induced degenerate *p*-doping can be presumably achieved *via* positive (oxidative) potential intercalation with specific anion or neutral molecules.

The transport properties of PTCDA-MoS_2 at various temperature have also been carried out to further test the influence of PTCDA intercalation on the contact barrier of MoS_2 device. As shown in Fig. 4c and 4d, the switching ratio of the FETs increases gradually during the temperature decrease, the on-current increases from 44.2 μA at 300 K to 119.8 μA at 50 K, and the carrier mobility increases from 96 cm^{-2} V^{-1} S^{-1} to 300 cm^{-2} V^{-1} S^{-1}, respectively. Additionally, a linear I-V output and ohmic behavior of PTCDA intercalated MoS_2 remains down to 50K (see Fig. S11), indicating an excellent barrier free contact at cryogenic temperatures. The degenerate doping and contact barrier elimination can be attributed to charge transfer between PTCDA and MoS_2, and therefore provides a good basis for the further construction of functionalized heterojunctions and other comprehensive device structures.

We further noticed that the on-chip intercalation of PTCDA molecules follows a long-range reaction behavior, where the molecules seem to travel along the entire 2D crystals regardless of the intercalation point (exposed electrochemical window), even at a distant location, as shown in Fig. S12. To utilize such distinct behavior, a Si-MoS_2 vertical junction was fabricated and PTCDA modulation was employed to construct a complicate vertical vdW heterostructure with a presumable molecular tunneling junction. The few-layered MoS_2 was first transferred onto highly *p*-doping Si surface (etched SiO_2 region), to form a *p-n* junction, with contact metal deposited on each side (fabrication details can be found in Supplementary Methods and Fig. S13. As shown in Figure 4c, the active electrochemical window (initial point for intercalation) of Si-MoS_2 diode was then opened at a distant location from the Si-MoS_2 vertical junction (see Fig. S14) for SEM and OM images. This schematic could potentially be applied to many complex vertical heterostructures where the intercalation (reaction) point can be separate from the active device area (or have to if the target 2D layer is covered and therefore isolated by other layers), preventing the possible decomposition or contamination of any layers in a heterostructure. Upon PTCDA intercalation, I-V curve changes from a typical *p-n* diode characteristic, to an obvious symmetrical behavior, with significantly enhanced current density. This result matches the transport behavior of a typical tunneling diode,[44, 45] which can be attributed to the molecular PTCDA layer within the MoS_2-PTCDA-MoS_2 heterostructure, as illustrated in Figure 4f inset. The MoS_2-PTCDA-MoS_2 tunneling junction can further function as a molecular tunneling transistor,[45] operated at the room temperature. When applied with varying ionic gate voltages *via* ionic liquid (DEME-TFSI), the tunneling current shows a clear electric field modulation, with a current density up to 10^1 A cm^{-2} (see Fig. S15). Successful development of the vertical molecular tunneling transistor further highlights the merit of our long-range intercalation approach to create

artificial heterojunctions based on 2D atomic crystal and functional molecule monolayer that are difficult to fabricate through layer-by-layer integration.[7]

CONCLUSIONS

In summary, we have demonstrated an on-chip electrochemical intercalation strategy that enables vdW integration of inorganic/organic heterostructures from typical 2D atomic crystals and organic semiconductor molecules. Through systematic characterizations and transport measurements, especially STEM cross-sectional imaging and EELS that revealed structural, elemental and band electronic information at layer-by-layer resolution, we confirmed strong electronic coupling between inorganic/organic layers in the artificial heterostructure of MoS_2/PTCDA, along with the modulation of electronic/opto properties. The same approach has also been successfully applied to a variety of 2DLMs and semiconductor organic molecules. Our study defines a versatile platform of inorganic/organic heterostructure/superlattices with vast potential functionalities originated from molecules layers by design, including electronic/photonic properties from semiconductor molecules with well-defined HOMO/LUMO, magnetic properties from electron spins in radicals or coordination compounds, and symmetry-breaking (of 2D atomic crystal) features from asymmetric compounds. The long-range intercalation can also enable the non-local modulation for complicated junctions, and provides an effective path for vertical molecular tunneling transistors sandwiched by 2D contacts. Overall, this strategy will significantly promote the functional device design and fabrication for next-generation nanoelectronics and quantum devices with potentially distinct spin-orbit coupling.

EXPERIMENTAL SECTIONS

Device fabrication: The fabrication of the *n*-MoS_2 FETs were obtained by mechanical exfoliation from bulk crystal onto a doped Si substrate with 275nm SiO_2. The substrate was

identified by using an optical microscope (Olympus) with a color camera. Metallic contacts were prepared using e-beam lithography (Tescan Vega 3) and e-beam evaporation (Kurt Lesker) of Ti (20 nm) and Au (50 nm). Small cell for electrochemical intercalation was prepared by spin-coating PMMA (A8, MicroChem Crop.) on the substrate to form an electrochemically inert thin film, with following e-beam lithography to open an electrochemical active window to avoid electrochemical reactions on the metal electrode.

On-chip electrochemical intercalation: Pre-fabricated two-terminal MoS_2 device was incorporated into an on-chip three-electrochemical cell, with MoS_2 channel as working electrode (WE), Pt wire as counter electrode (CE), and leak-free Ag/AgCl as reference electrode (RE, Harvard Apparatus LF-2). Intercalant (PTCDA) was dissolved in organic solvents (DMSO) and used as electrolyte. The active electrochemical area was defined by an electrochemically inert polydimethylsiloxane (PDMS) window prepared using electron beam lithography (EBL) to avoid the reaction from source/drain electrode. For intercalation, a two-channel source-drain-unit (SMU, Agilent 2902a) was employed, one for applying electrochemical potential (V_g) and collecting the gate Faradic current (I_g, corresponding to the electrochemical current in a typical cyclic voltammetry (CV)), and the other for *in situ* electrical measurement of the MoS_2 channel (lateral), *i.e.*, ETS signals. One channel was used to precisely control the electrochemical potential and scan rate was 100 mV s^{-1}, and the other channel was used to apply a bias (50 mV) and to measure the channel conducting current between source and drain (I_{ds}).

Microscopic Characterization: High resolution STEM-HAADF image was obtained on a double spherical aberration (Cs)-corrected S/TEM FEI Titan G2 60-300 at 300 kV with a field emission gun. The probe convergence angle was 25 mrad, and the angular range of the HAADF detector was from 79.5 mrad to 200 mrad. STEM-EELS spectral imaging was performed on a

Gatan Quantum 966 system, and the 2D atomic level EELS mappings were conducted with the monochromator off. The energy loss near-edge structures (ELNES) were used to study the local electronic structure at a sub-u.c. resolution using an energy resolution of approximately 1.2 eV, and the dwell time for recording each spectrum was 0.1 s with a collection semiangle of 36 mrad.

ASSOCIATED CONTENTS

Supporting Information Available:

The Supporting Information is available free of charge on the ACS Publications website at DOI: Additional information on experiment details, spectroscopic and microscopic characterizations, electrochemical studies, and intercalation results of other TMDs and semiconductor organic molecules.

Conflict of Interest: The authors declare no competing financial interest.

ACKNOWLEDGEMENTS

M.D. acknowledges the support by the Fundamental Research Funds for the Central Universities in China (020514380136 and 020514380195), Natural Science Foundation of Jiangsu Province (BK20180321), and instrument/technical support from State Key Lab of Analytical Chemistry for Life Science, and State Key Lab of Coordination Chemistry. P.W. S.C acknowledge funding from the National Natural Science Foundation of China (11874199), the National Basic Research Program of China, (Grant No. 2015CB654901); X.W acknowledges funding support by National Natural Science Foundation of China 61734003, 61521001, 51861145202, 61861166001, 61851401, National Key Basic Research Program of China 2015CB921600, Strategic Priority

Research Program of Chinese Academy of Sciences XDB 30000000, and the Fundamental Research Funds for the Central Universities, China; S. H. C. acknowledges the support by the Program A for Outstanding Ph.D. candidate of Nanjing University (201801A013) and Postgraduate Research & Practice Innovation Program of Jiangsu Province (KYCX18_0045).

AUTHOR CONTRIBUTIONS

M.D., P.W. and X.W. designed the research, directed and supervised the research; W.H. conducted the device fabrication, intercalation experiments, spectroscopic characterizations and data analysis; H.Z. contributed to device fabrication, spectroscopic characterization, and sample preparation for structural analysis; S.C. conducted experiments and data analysis for structural and elemental characterization of the superlattice; Z.M. contributed to device fabrication. M.D. and W.H. co-wrote the manuscript; All authors discussed the results and commented on the manuscript.

REFERENCES

(1) Radisavljevic, B.; Radenovic, A.; Brivio, J.; Giacometti, V.; Kis, A., Single-layer MoS_2 Transistors. *Nat. Nanotechnol.* **2011**, *6*, 147-150.

(2) Wu, W.; Wang, L.; Li, Y.; Zhang, F.; Lin, L.; Niu, S.; Chenet, D.; Zhang, X.; Hao, Y.; Heinz, T. F.; Hone, J.; Wang, Z. L., Piezoelectricity of Single-atomic-layer MoS_2 for Energy Conversion and Piezotronics. *Nature* **2014**, *514*, 470-474.

(3) Lopez-Sanchez, O.; Lembke, D.; Kayci, M.; Radenovic, A.; Kis, A., Ultrasensitive Photodetectors Based on Monolayer MoS_2. *Nat. Nanotechnol.* **2013**, *8*, 497-501.

(4) Sarkar, D.; Liu, W.; Xie, X.; Anselmo, A. C.; Mitragotri, S.; Banerjee, K., MoS_2 Field-effect Transistor for Next-generation Label-free Biosensors. *ACS Nano* **2014**, *8*, 3992-4003.

(5) Cui, S.; Pu, H.; Wells, S. A.; Wen, Z.; Mao, S.; Chang, J.; Hersam, M. C.; Chen, J., Ultrahigh Sensitivity and Layer-dependent Sensing Performance of Phosphorene-based Gas Sensors. *Nat. Commun.* **2015**, *6*, 8632.

(6) Geim, A. K.; Grigorieva, I. V., Van der Waals Heterostructures. *Nature* **2013**, *499*, 419-425.

(7) Liu, Y.; Weiss, N. O.; Duan, X.; Cheng, H.-C.; Huang, Y.; Duan, X., Van der Waals Heterostructures and Devices. *Nat. Rev. Mater.* **2016**, *1*.

(8) Liu, Y.; Huang, Y.; Duan, X., Van der Waals Integration Before and Beyond Two-dimensional Materials. *Nature* **2019**, *567*, 323-333.

(9) Zhang, J.; Yang, A.; Wu, X.; van de Groep, J.; Tang, P.; Li, S.; Liu, B.; Shi, F.; Wan, J.; Li, Q.; Sun, Y.; Lu, Z.; Zheng, X.; Zhou, G.; Wu, C. L.; Zhang, S. C.; Brongersma, M. L.; Li, J.; Cui, Y., Reversible and Selective Ion Intercalation through the Top Surface of Few-layer MoS_2. *Nat. Commun.* **2018**, *9*, 5289.

(10) Gong, Y.; Yuan, H.; Wu, C. L.; Tang, P.; Yang, S. Z.; Yang, A.; Li, G.; Liu, B.; van de Groep, J.; Brongersma, M. L.; Chisholm, M. F.; Zhang, S. C.; Zhou, W.; Cui, Y., Spatially Controlled Doping of Two-dimensional SnS_2 through Intercalation for Electronics. *Nat. Nanotechnol.* **2018**, *13*, 294-299.

(11) Cho, S.; Kim, S.; Kim, J. H.; Zhao, J.; Seok, J.; Keum, D. H.; Baik, J.; Choe, D.-H.; Chang, K. J.; Suenaga, K., Phase Patterning for Ohmic Homojunction Contact in $MoTe_2$. *Science* **2015**, *349*, 625-628.

(12) Yu, Y.; Nam, G. H.; He, Q.; Wu, X. J.; Zhang, K.; Yang, Z.; Chen, J.; Ma, Q.; Zhao, M.;

Liu, Z.; Ran, F. R.; Wang, X.; Li, H.; Huang, X.; Li, B.; Xiong, Q.; Zhang, Q.; Liu, Z.; Gu, L.; Du, Y., et al., High Phase-purity 1T'-MoS_2- and 1T'-$MoSe_2$-layered Crystals. *Nat. Chem.* **2018**, *10*, 638-643.

(13) Kiriya, D.; Tosun, M.; Zhao, P.; Kang, J. S.; Javey, A., Air-stable Surface Charge Transfer Doping of MoS_2 by Benzyl Viologen. *J. Am. Chem. Soc.* **2014**, *136*, 7853-7856.

(14) Tarasov, A.; Zhang, S.; Tsai, M. Y.; Campbell, P. M.; Graham, S.; Barlow, S.; Marder, S. R.; Vogel, E. M., Controlled Doping of Large-area Trilayer MoS_2 with Molecular Reductants and Oxidants. *Adv. Mater.* **2015**, *27*, 1175-1181.

(15) Shin, H.-J.; Choi, W. M.; Choi, D.; Han, G. H.; Yoon, S.-M.; Park, H.-K.; Kim, S.-W.; Jin, Y. W.; Lee, S. Y.; Kim, J. M., Control of Electronic Structure of Graphene by Various Dopants and Their Effects on a Nanogenerator. *J. Am. Chem. Soc.* **2010**, *132*, 15603-15609.

(16) Gong, C.; Zhang, X., Two-dimensional Magnetic Crystals and Emergent Heterostructure Devices. *Science* **2019**, *363*, eaav4450.

(17) Fang, H.; Battaglia, C.; Carraro, C.; Nemsak, S.; Ozdol, B.; Kang, J. S.; Bechtel, H. A.; Desai, S. B.; Kronast, F.; Unal, A. A.; Conti, G.; Conlon, C.; Palsson, G. K.; Martin, M. C.; Minor, A. M.; Fadley, C. S.; Yablonovitch, E.; Maboudian, R.; Javey, A., Strong Interlayer Coupling in van der Waals Heterostructures Built from Single-layer Chalcogenides. *Proc. Natl. Acad. Sci. USA* **2014**, *111*, 6198-6202.

(18) Cui, X.; Shih, E. M.; Jauregui, L. A.; Chae, S. H.; Kim, Y. D.; Li, B.; Seo, D.; Pistunova, K.; Yin, J.; Park, J. H.; Choi, H. J.; Lee, Y. H.; Watanabe, K.; Taniguchi, T.; Kim, P.; Dean, C. R.; Hone, J. C., Low-Temperature Ohmic Contact to Monolayer MoS_2 by van der Waals Bonded Co/h-BN Electrodes. *Nano Lett.* **2017**, *17*, 4781-4786.

(19) Wang, M.; Cai, S.; Pan, C.; Wang, C.; Lian, X.; Zhuo, Y.; Xu, K.; Cao, T.; Pan, X.; Wang,

B., Robust Memristors Based on Layered Two-dimensional Materials. *Nat. Electron.* **2018**, *1*, 130.

(20) Bediako, D. K.; Rezaee, M.; Yoo, H.; Larson, D. T.; Zhao, S. Y. F.; Taniguchi, T.; Watanabe, K.; Brower-Thomas, T. L.; Kaxiras, E.; Kim, P., Heterointerface Effects in the Electrointercalation of van der Waals Heterostructures. *Nature* **2018**, *558*, 425-429.

(21) Chen, Z.; Leng, K.; Zhao, X.; Malkhandi, S.; Tang, W.; Tian, B.; Dong, L.; Zheng, L.; Lin, M.; Yeo, B. S.; Loh, K. P., Interface Confined Hydrogen Evolution Reaction in Zero Valent Metal Nanoparticles-intercalated Molybdenum Disulfide. *Nat. Commun.* **2017**, *8*, 14548.

(22) Wan, C.; Gu, X.; Dang, F.; Itoh, T.; Wang, Y.; Sasaki, H.; Kondo, M.; Koga, K.; Yabuki, K.; Snyder, G. J.; Yang, R.; Koumoto, K., Flexible *n*-type Thermoelectric Materials by Organic Intercalation of Layered Transition Metal Dichalcogenide TiS_2. *Nat. Mater.* **2015**, *14*, 622-627.

(23) Wang, C.; He, Q.; Halim, U.; Liu, Y.; Zhu, E.; Lin, Z.; Xiao, H.; Duan, X.; Feng, Z.; Cheng, R.; Weiss, N. O.; Ye, G.; Huang, Y. C.; Wu, H.; Cheng, H. C.; Shakir, I.; Liao, L.; Chen, X.; Goddard, W. A., III; Huang, Y., *et al*., Monolayer Atomic Crystal Molecular Superlattices. *Nature* **2018**, *555*, 231-236.

(24) Lin, Z.; Liu, Y.; Halim, U.; Ding, M.; Liu, Y.; Wang, Y.; Jia, C.; Chen, P.; Duan, X.; Wang, C.; Song, F.; Li, M.; Wan, C.; Huang, Y.; Duan, X., Solution-processable 2D Semiconductors for High-performance Large-area Electronics. *Nature* **2018**, *562*, 254-258.

(25) He, Q.; Lin, Z.; Ding, M.; Yin, A.; Halim, U.; Wang, C.; Liu, Y.; Cheng, H.-C.; Huang, Y.; Duan, X., *In Situ* Probing Molecular Intercalation in Two-Dimensional Layered Semiconductors. *Nano Lett.* **2019**, *19*, 6819-6826.

(26) Kappera, R.; Voiry, D.; Yalcin, S. E.; Branch, B.; Gupta, G.; Mohite, A. D.; Chhowalla, M., Phase-engineered Low-resistance Contacts for Ultrathin MoS_2 Transistors. *Nat. Mater.* **2014**,

13, 1128-1134.

(27) Gangilenka, V. R.; Titova, L. V.; Smith, L. M.; Wagner, H. P.; DeSilva, L. A. A.; Gisslén, L.; Scholz, R., Selective Excitation of Exciton Transitions in PTCDA Crystals and Films. *Adv. Funct. Mater.* **2010**, *81*.

(28) Ding, M.; He, Q.; Wang, G.; Cheng, H. C.; Huang, Y.; Duan, X., An on-chip Electrical Transport Spectroscopy Approach for *In Situ* Monitoring Electrochemical Interfaces. *Nat. Commun.* **2015**, *6*, 7867.

(29) Ding, M.; Shiu, H. Y.; Li, S. L.; Lee, C. K.; Wang, G.; Wu, H.; Weiss, N. O.; Young, T. D.; Weiss, P. S.; Wong, G. C.; Nealson, K. H.; Huang, Y.; Duan, X., Nanoelectronic Investigation Reveals the Electrochemical Basis of Electrical Conductivity in Shewanella and Geobacter. *ACS Nano* **2016**, *10*, 9919-9926.

(30) Ding, M.; Zhong, G.; Zhao, Z.; Huang, Z.; Li, M.; Shiu, H. Y.; Liu, Y.; Shakir, I.; Huang, Y.; Duan, X., On-Chip *In Situ* Monitoring of Competitive Interfacial Anionic Chemisorption as a Descriptor for Oxygen Reduction Kinetics. *Acs Cent. Sci.* **2018**, *4*, 590-599.

(31) Perera, M. M.; Lin, M.-W.; Chuang, H.-J.; Chamlagain, B. P.; Wang, C.; Tan, X.; Cheng, M. M.-C.; Tománek, D.; Zhou, Z., Improved Carrier Mobility in Few-layer MoS_2 Field-effect Transistors with Ionic-liquid Gating. *ACS Nano* **2013**, *7*, 4449-4458.

(32) Li, H.; Zhang, Q.; Yap, C. C. R.; Tay, B. K.; Edwin, T. H. T.; Olivier, A.; Baillargeat, D., From Bulk to Monolayer MoS_2: Evolution of Raman Scattering. *Adv. Funct. Mater.* **2012**, *22*, 1385-1390.

(33) Zhanpeisov, N. U.; Nishio, S.; Fukumura, H., Density Functional Theory Study of Vibrational Properties of the 3,4,9,10-perylene tetracarboxylic dianhydride (PTCDA) Molecule: IR, Raman, and UV-vis Spectra. *Int. J. Quantum Chem.* **2005**, *105*, 368-375.

(34) Lin, J. D.; Han, C.; Wang, F.; Wang, R.; Xiang, D.; Qin, S.; Zhang, X.-A.; Wang, L.; Zhang, H.; Wee, A. T. S., Electron-doping-enhanced Trion Formation in Monolayer Molybdenum Disulfide Functionalized with Cesium Carbonate. *ACS Nano* **2014**, *8*, 5323-5329.

(35) Eda, G.; Yamaguchi, H.; Voiry, D.; Fujita, T.; Chen, M.; Chhowalla, M., Photoluminescence from Chemically Exfoliated MoS_2. *Nano Lett.* **2011**, *11*, 5111-5116.

(36) Hestand, N. J.; Spano, F. C., Expanded Theory of H-and J-molecular Aggregates: the Effects of Vibronic Coupling and Intermolecular Charge Transfer. *Chem. Rev.* **2018**, *118*, 7069-7163.

(37) Kaushik, N.; Karmakar, D.; Nipane, A.; Karande, S.; Lodha, S., Interfacial *n*-Doping Using an Ultrathin TiO_2 Layer for Contact Resistance Reduction in MoS_2. *ACS Appl. Mater. Interfaces* **2016**, *8*, 256-263.

(38) Das, S.; Chen, H. Y.; Penumatcha, A. V.; Appenzeller, J., High Performance Multilayer MoS_2 Transistors with Scandium Contacts. *Nano Lett.* **2013**, *13*, 100-105.

(39) Ji, D.; Cai, S.; Paudel, T. R.; Sun, H.; Zhang, C.; Han, L.; Wei, Y.; Zang, Y.; Gu, M.; Zhang, Y., Freestanding Crystalline Oxide Perovskites Down to the Monolayer Limit. *Nature* **2019**, *570*, 87.

(40) Wang, Y.; Kim, J. C.; Wu, R. J.; Martinez, J.; Song, X.; Yang, J.; Zhao, F.; Mkhoyan, A.; Jeong, H. Y.; Chhowalla, M., van der Waals Contacts Between Three-dimensional Metals and Two-dimensional Semiconductors. *Nature* **2019**, *568*, 70-74.

(41) Lin, Y. C.; Dumcenco, D. O.; Huang, Y. S.; Suenaga, K., Atomic Mechanism of the Semiconducting-to-metallic Phase Transition in Single-layered MoS_2. *Nat. Nanotechnol.* **2014**, *9*, 391-396.

(42) Martin, J. M.; Vacher, B.; Ponsonnet, L.; Dupuis, V., Chemical Bond Mapping of Carbon

by Image-spectrum EELS in the Second Derivative Mode. *Ultramicroscopy* **1996**, *65*, 229-238.

(43) W. Li, J. Zhou, S. Cai, Z. Yu, J. Zhang, N. Fang, T. Li, Y. Wu, T. Chen, X. Xie, H. Ma, K. Yan, N. Dai, X. Wu, H. Zhao, Z. Wang, D. He, L. Pan, Y. Shi, P. Wang, *et al*., Uniform and Ultrathin High-κ Gate Dielectrics for Two-Dimensional Electronic Devices. *Nat. Electron.* **2019**, *2*, 563.

(44) Liu, Y.; Yuan, L.; Yang, M.; Zheng, Y.; Li, L.; Gao, L.; Nerngchamnong, N.; Nai, C. T.; Sangeeth, C. S.; Feng, Y. P.; Nijhuis, C. A.; Loh, K. P., Giant Enhancement in Vertical Conductivity of Stacked CVD Graphene Sheets by Self-assembled Molecular Layers. *Nat. Commun.* **2014**, *5*, 5461.

(45) Jia, C.; Famili, M.; Carlotti, M.; Liu, Y.; Wang, P.; Grace, I. M.; Feng, Z.; Wang, Y.; Zhao, Z.; Ding, M., Quantum Interference Mediated Vertical Molecular Tunneling Transistors. *Sci. Adv.* **2018**, *4*, eaat8237.